JOURNAL OF GEOPHYSICAL RESEARCH, VOL. 112, C10015, doi:10.1029/2006JC003841, 2007

Full-scale observations of wave-induced vortex generation over a rippled bed

C. S. Nichols[1] and D. L. Foster[1]

Received 26 July 2006; revised 7 March 2007; accepted 30 May 2007; published 13 October 2007.

[1] Our understanding of vortex generation over rippled beds is largely based on small-scale laboratory studies. The insight provided by such studies has been considerable, although questions remain regarding the applicability to the field. This paper presents observations from a full-scale investigation of wave-induced vortex generation events over a movable sediment bed. Observations of the two-dimensional time varying velocity field were obtained with a submersible Particle Image Velocimetry (PIV) system in a field-scale, experimental environment at the O. H. Hinsdale Wave Research Laboratory. The observations were obtained over an irregularly rippled bed with ripple height and wavelength of roughly 0.01 m and 0.1 m, respectively. The vortices generated during offshore directed flow over the steeper bed form slope were regularly ejected into the water column and were consistent with conceptual models of the oscillatory flow over a backward facing step. The observations allowed for an examination of the generation and subsequent ejection of individual vortical structures. Vortical structures are identified with a measure of the flow field that estimates the time for a complete revolution of a vortex called swirling strength. An analysis of these structures reveals that the swirling strength nondimensionalized by the wave period is correlated to the Keulegan-Carpenter. These results offer new insight into fluid sediment interaction over rippled beds.

Citation: Nichols, C. S., and D. L. Foster (2007), Full-scale observations of wave-induced vortex generation over a rippled bed, *J. Geophys. Res.*, *112*, C10015, doi:10.1029/2006JC003841.

1. Introduction

[2] Investigations empirically relating vortex shedding over rippled beds to oscillatory flows date back to *Darwin* [1883] and *Bagnold* [1946]. Through a series of empirical studies, these two pioneers suggested that vortices form on the lee side of ripples and are capable of suspending sediment if the hydrodynamic conditions remain within a limited window. Photographic and hot-wire observations by *Nakato et al.* [1977] and *Honji et al.* [1980] later confirmed the Darwin and Bagnold hypotheses. The investigations also showed vortices that separate from the bed are capable of advecting sediment [*Honji et al.*, 1980] and that this ejection occurs as the velocity passes through zero [*Nakato et al.*, 1977]. Recently, more detailed observations of vortex shedding induced by oscillatory motions have been made in a series of small-scale laboratory experiments [e.g., *Earnshaw and Greated*, 1998; *Ahmed and Sato*, 2001; *Sand Jespersen et al.*, 2004; *Ourmieres and Chaplin*, 2004]. Most of these observations were obtained over fixed beds in laminar or transitionally turbulent flow (see Table 1 for a summary of the experimental parameters). The vortical structures in transitionally turbulent flow were shown to reach maximum strength at 90 degrees when the horizontal velocity is largest [*Earnshaw and Greated*, 1998]. In the only free-surface wave examination of the available observations, *Earnshaw and Greated* [1998] also found negative vortices generated by onshore-directed flow, to be stronger than positive vortices generated by offshore-directed flow. In transitionally turbulent flow, *Ourmieres and Chaplin* [2004] observed that vortex ejection was a function of the Taylor number, confirming the findings of *Hara and Mei* [1990]. These observations have provided considerable detail and insight; however, questions remain regarding the applicability of these small-scale observations to fully turbulent flow at field scale.

[3] Field-scale observations of fluid-sediment interactions over rippled beds have primarily been limited to one-dimensional profiles of the water column, [e.g., *Osborne and Vincent*, 1996; *Thorne and Hanes*, 2002; *Smyth et al.*, 2002; *Chang and Hanes*, 2004; *Foster et al.*, 2007]. These observations have shown significantly different wave bottom boundary layer characteristics for a range of bed geometries. For example, *Smyth et al.* [2002] observed that irregular ripples exhibit the largest magnitudes of near-bed turbulence, reinforcing the idea that vortex shedding may play a significant role in the wave bottom boundary layer dynamics.

[4] The objective of this effort is to provide evidence of vortex generation and ejection over movable rippled beds in a full-scale, free surface wave environment. Field-scale laboratory observations of the lowest 0.23 m of the water column are obtained with new particle image velocimetry

[1]Department of Civil and Environmental Engineering and Geodetic Science, Ohio State University, Columbus, Ohio, USA.

0148-0227/07/2006JC003841$09.00

Table 1. Summary of Previous and Current Experimental Parameters

Paper	U_{max}, m/s	T, s	Re, $\times 10^4$	KC	Wave Condition	d_{50}, mm	η_b, m	λ_b, m
Sand Jespersen et al. [2004]	0.079, 0.145	2	0.22, 0.75	3.16	rigid lid sinusoidal	N/A	0.05	0.10
Ourmieres and Chaplin [2004]	...	1–3.14	0.2–1.0	...	free surface sinusoidal	N/A	0.002, 0.004, 0.0048, 0.009	0.04, 0.0514
Ahmed and Sato [2001]	0.48	3	12	72	rigid lid asymmetric	0.2	0.02	0.16
Earnshaw and Greated [1998] (setup 1)	0.13, 0.20, 0.294	8.46	2.3, 5.4, 11	31, 48, 71	rigid lid sinusoidal	N/A	0.035	0.22
Earnshaw and Greated [1998] (setup 2)	0.28	2.5	3.5	20	free surface sinusoidal	N/A	0.035	0.22
Current effort 2006	1.1	6	$\leq$60	456	free surface random	0.2	0.01	0.1

(PIV) observations. While PIV has been used extensively in controlled lab environments [e.g., *Adrian*, 1991; *Willert and Gharib*, 1991; *Rockwell et al.*, 1993; *Adrian*, 2005], it has only recently been deployed in the ocean environment [e.g., *Nimmo Smith et al.*, 2002, 2004]. In the nearshore, such observations are complicated by the dynamic nature of the bed, unpredictable optical quality of the water, and generally harsh wave environment. These observations are the first full-scale observations of the two-dimensional time-varying flow field dynamics over movable rippled beds.

2. Observations

[5] The observations for this effort were obtained during the summer of 2005 as part of the collaborative CROss Shore Sediment Transport EXperiment (CROSSTEX). The experiment was performed in the Large Wave Flume (LWF) at the O. H. Hinsdale Wave Research Laboratory at Oregon State University. The LWF is 104 m long, 3.7 m wide, and 4.6 m deep, with a programmable, hinged-type hydraulic ram wave generator capable of producing oscillatory flows and simulating regular, as well as random, wave groups. The offshore wave conditions in this study were defined with a TMA spectrum specified with a significant wave height (H_{mo}), wave period (T), and spectrum spread (γ) of 0.4 m, 6 s, and 10, respectively. At approximately 30 m offshore, with a still water depth of 1.6 m, this resulted in a root-mean-square horizontal velocity, u_{RMS}, of 0.24 m/s and a mean horizontal velocity, u_{mean}, of -0.3 m/s at an elevation of 0.6 m from the bed. Positive velocity is directed in the onshore and upward directions. The median grain size at the sampling location was 0.2 mm.

[6] Five independent, 48-s PIV realizations were obtained within a 7.5-min duration of the 20-min wave run (Table 2). An Acoustic Doppler Velocimeter (ADV) sampled the free stream velocity at 25 Hz at an elevation of 0.62 m from the bed (Figure 1). Observations of the two-dimensional (x-z) flow field and bed geometry were obtained with a submersible Dantec PIV system. A 120 mJ Nd:Yag laser was located 0.7 m above the bed and illuminated a vertical (x-z) slice of the water column (Figure 1). An obliquely oriented 1 megapixel digital camera secured to the flume wall obtained 48-s bursts of image pairs over a 0.23 m $\times$ 0.23 m approximate area (x-z) of interest. Image pairs were collected at a 15 Hz sampling rate with a 3 ms temporal lag between image pair members. The remotely controlled camera had aScheimpflug adjustment to orient the camera lens perpendicularly to the laser sheet. Seeding material included natural organic material as well as entrained sediment. Two-dimensional velocity fields were calculated with adaptive correlations of 32 $\times$ 32 pixel windows with a 50% overlap in a manner consistent with *Nimmo Smith et al.* [2004]. At a velocity of 0.50 m/s, particles will travel 2 mm or approximately 25% of the interrogation window. Unresolved velocity vectors result from one of the following three situations: (1) when the number of scatters is too low; (2) when the near-bed sediment concentration is too large or there is a large reflection from the bed; and (3) in the low-illumination part of the image that is focused on the bed between the laser plane and the camera.

3. Results

[7] The mean bed elevation over each of the five 48-s realizations was assumed to be the centroid of the light reflected from the bed of the mean image (see Figure 2 for an example of the mean image for the second realization). The region of the image below the high-intensity bed reflection is the water-sediment interface located between the laser sheet and the camera. This region is outside the

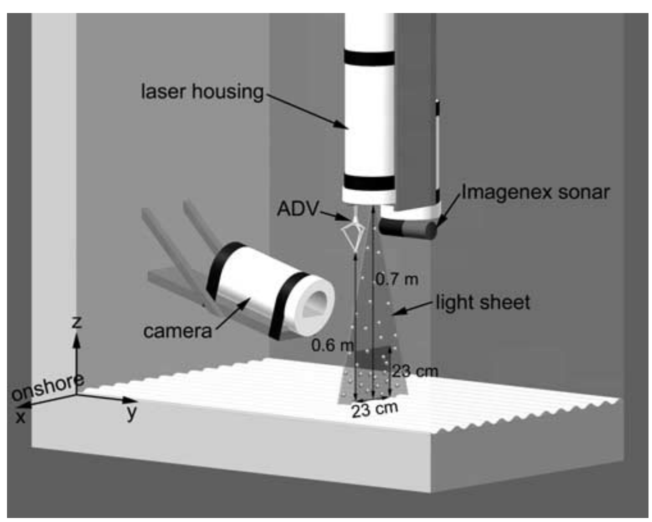

Figure 1. Schematic diagram of the submersible observation system.

Table 2. Statistics for Each of the Realizations

Realization	t_{start}, s	t_{end}, s	$U_{rms_{PIV}}$, m/s	$U_{rms_{ADV}}$, m/s	R^2	Migration Rate, m/s	$U_{peak_{PIV}}$, m/s	Uncertainty, m/s (% of peak)
1	491	539	0.28	0.27	0.98	...	0.91	±0.078 (±9%)
2	585	633	0.29	0.27	0.97	0.0005	1.07	±0.098 (±9%)
3	681	729	0.25	0.24	0.99	0.0001	0.82	±0.057 (±7%)
4	783	831	0.23	0.22	0.98	0.0003	0.91	±0.073 (±8%)
5	888	936	0.24	0.22	0.99	0.0003	1.04	±0.065 (±7%)

plane of the laser sheet and consequently the correlations are low and all velocity estimates are neglected. The upper and lower bounds of the bed reflection were defined as the elevation at 95% of the maximum light intensity. These values were less than 6 mm from the mean bed elevation (Figure 2a). Over the course of the five realizations, the bed form maintained its general shape with a wavelength, λ_b, of roughly 0.1 m and ripple height, η_b ranging from 0.01 to 0.015 m, but migrated onshore at a rate varying from 0.0001 to 0.0005 m/s (0.01 to 0.05 cm/s). Table 2 gives bed form migration rates for individual realizations.

[8] Figure 2 also shows the root-mean-square (RMS) flow field calculated for all valid vectors over the second realization. There exists a relatively small boundary layer

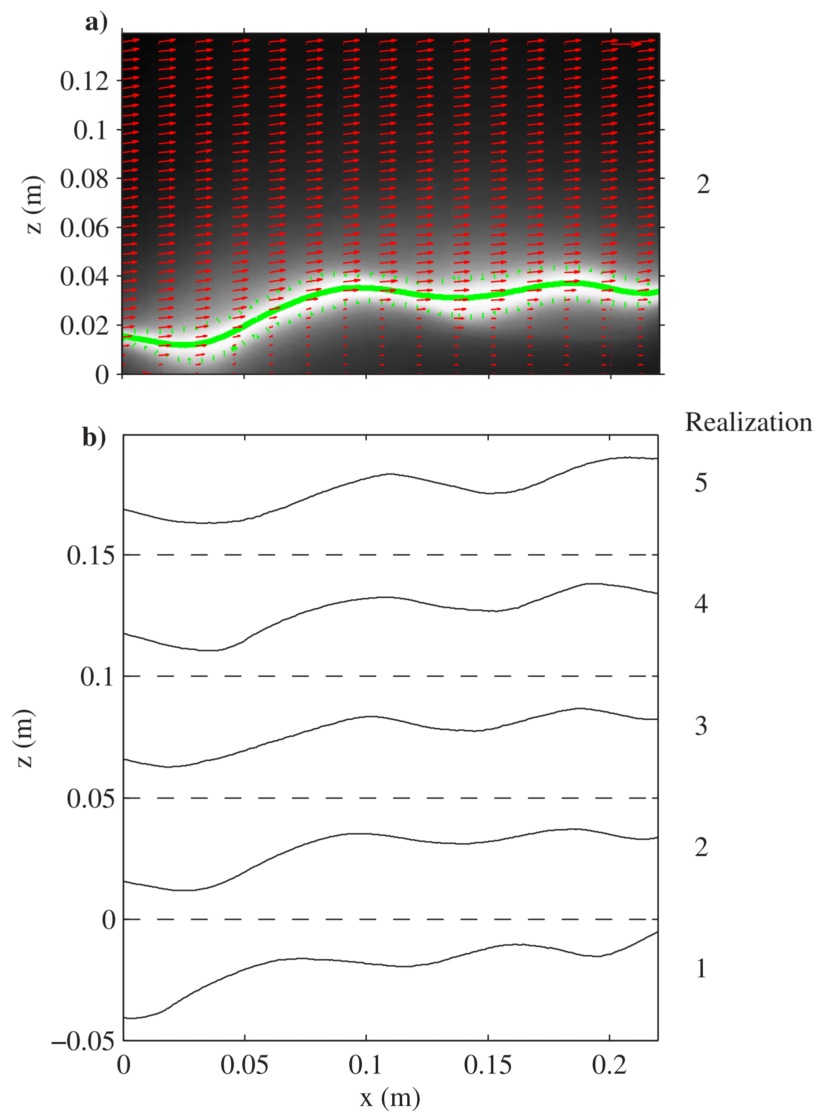

Figure 2. (a) Mean image intensity over the second 48-s PIV realization with the root-mean-square velocity field, u_{rms} (red vectors). The solid line shows the position of the centroid of the light reflected from the bed. The dotted lines show upper and lower bounds of the bed reflection. (b) Mean bed elevation for each of the five realizations. Each bed profile is vertically offset by 0.05 m. Onshore flow is directed to the right.

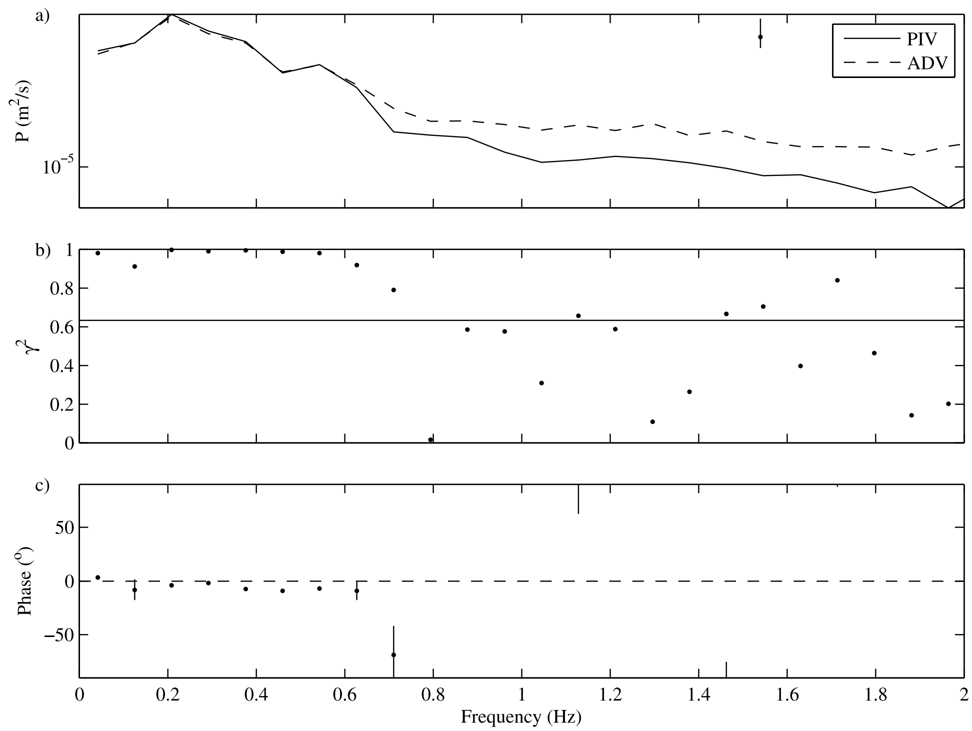

Figure 3. Horizontal velocity cross spectral analysis including the (a) power spectral density, (b) coherence, and (c) phase separation of U_{ADV} (dashed line) and U_{PIV} (solid line).

thickness that varies over the bed form. The boundary layer shows its thickest profile, 0.025 m, in the deepest bed form trough at x = 0.03 m. The observed wave bottom boundary layer thickness compares favorably to that of a 0.027-m layer thickness predicted only considering the grain roughness ($k_s = 2.5d_{50}$) by the *Madsen* [1994] empirical model that is derived from the *Grant and Madsen* [1979] eddy viscosity formulation. However, if the roughness is parameterized with the ripple geometry ($k_s = 27.7\ \eta_b^2/\lambda_b$) [*Grant and Madsen*, 1982], the predicted wave bottom boundary layer thickness of 0.05 to 0.07 m (depending on the ripple height assumed) is significantly larger than the observations. An examination of the nonnegligible root-mean-square velocities near the sediment-water interface offers a potential explanation for this disagreement. At the ripple crests, the RMS velocity at the approximate bed location is as large as 0.2 m/s and would clearly not satisfy a no-slip boundary condition as is generally assumed. These seemingly large velocity estimates may result from poor correlations at the actual water-sediment interface where there is a large light reflection. However, they are not inconsistent with the Duck94 field observations of *Foster et al.* [2000, 2006]. The Duck94 observations consisted of a vertical array of hot films placed in the wave bottom boundary layer and intermittently mobile sediment bed. The root-mean-square velocities at the bed ranged from 0.07 to 0.27 m/s under 5 s waves with a 0.35 m/s root-mean-square free stream wave velocity. These results also suggest that approximations of the wave bottom boundary dissipation, based on estimates of the shear velocity, u_*, would significantly overpredict the dissipation within the water column.

[9] A cross spectral analysis between the horizontal velocity as measured with the ADV (z = 0.6 m), U_{ADV}, and as measured with the PIV system at the center uppermost PIV vector (x = 0.11 m, z = 0.23 m), U_{PIV}, shows strong coherence that exceeds the 95% significance level at frequencies below 0.7 Hz (Figure 3b). Beyond 0.7 Hz, the drop in coherence may result from the reasonably high noise floor of the ADV sensor evident in Figure 3a. The two sensors are less than 10° out of phase at frequencies below 0.7 Hz (Figure 3c). A sample time series of U_{ADV} and U_{PIV} for the second realization is presented in Figure 4a. Following *Cowen et al.* [2003] and *Efron and Tibshirani* [1993], a bootstrap uncertainty interval at the 95% confidence level was determined for the random component for the uncertainty for the horizontal component of velocity. In these calculations, the ADV is assumed to be the true value of the free stream velocity. Because of a reasonably high noise floor (see Figure 3), the ADV signal was low-pass band filtered at 1 Hz (with a 40 point taper). Interpolation of these structures is also limited because the U_{ADV} and U_{PIV} were vertically offset by 0.42 m. The 95% uncertainty interval for the second realization was found to be ±0.098 m (±9% of the peak velocity). The mean correlation coefficient of the bootstrap analysis for the second realization was 0.99 ± 0.13 (see Table 2 for the uncertainty for each realization).

[10] Figure 4 shows the flow field and image evolution through two separate offshore directed flow excursions. Each sequence consists of velocity vectors and the image of the peak offshore flow (Figures 4b and 4e), followed by flow deceleration (Figures 4c and 4f), and flow reversal (Figures 4d and 4g). In all cases the instantaneous velocity

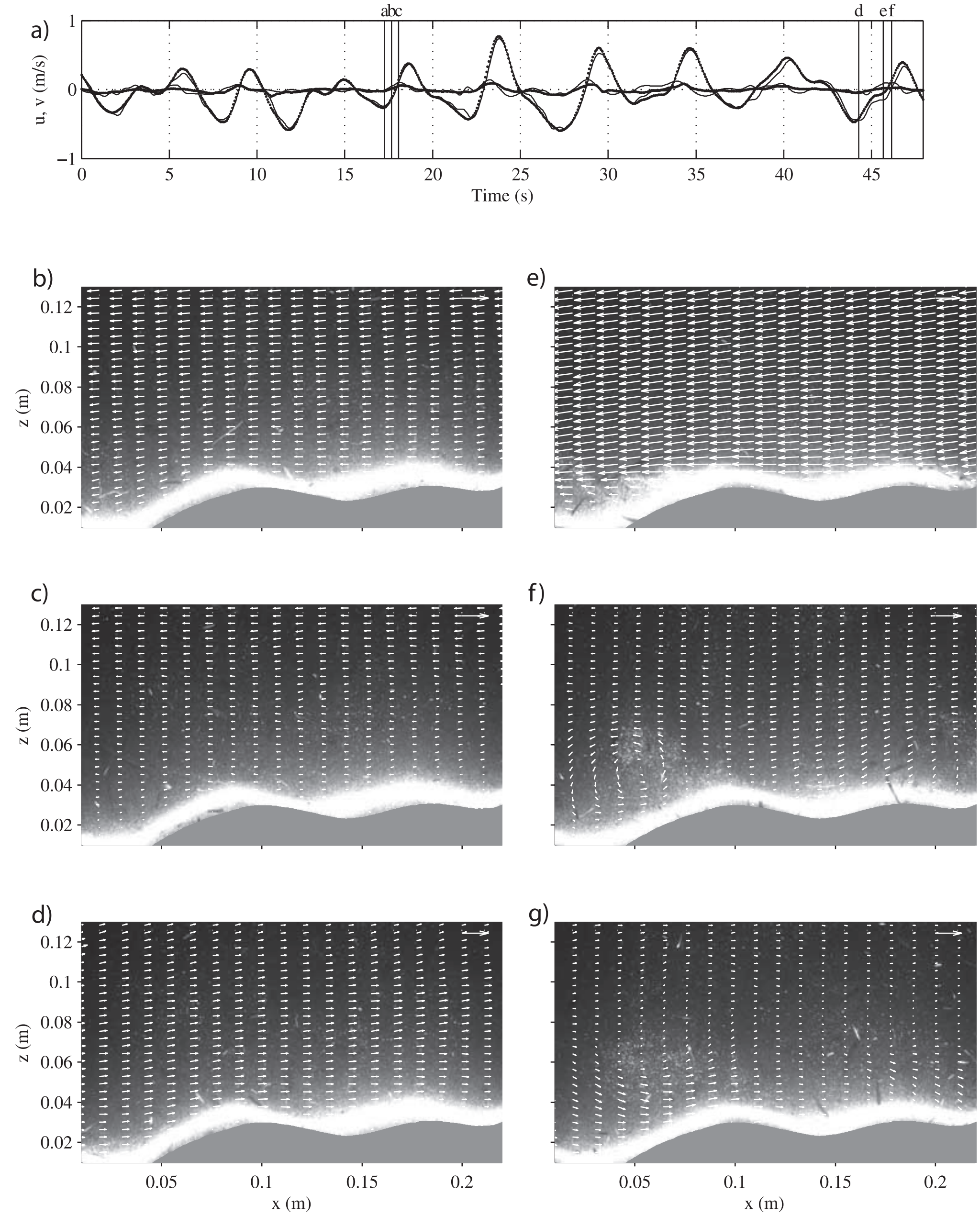

Figure 4. (a) A 48-s time series of horizontal and vertical velocities as measured by the ADV (solid line) and PIV (dots) for the second realization (see Figure 5 for colored direction differentiation). (b–g) Snapshots of the raw images and instantaneous velocity fields (white vectors) at the six times indicated in the time series in Figure 4a. A 0.5 m/s scale vector is shown in the upper right of each image. Onshore flow is directed to the right.

fields are mostly uniform above an elevation of 0.07 m from the reference elevation. In the first sequence, the peak offshore velocity reaches 0.15 m/s over a 1/2 wave excursion of 2.3 s (Figures 4b–4d). No noticeable vortical structure is evident and no coherent sediment plume is entrained into the water column during this reasonably low forcing excursion. In the second sequence, the peak offshore velocity reaches 0.44 m/s over a 1/2 wave excursion of 3.3 s (Figures 4e–4g). As the flow decelerates (Figure 4e), the near-bed flow at the steep slope of the most-offshore ripple (x = 0.05 m) separates and a vortex is formed. At this time, a sediment plume (shown by the higher-intensity particles) is entrained into the structure. In Figure 4g, the free stream velocity is zero and the phase lead of the wave bottom boundary layer is evident as the vortex and entrained sediment is released into the water column and advected with the flow (Figures 4b and 4e).

[11] Following *Sveen* [2004], the time-varying vorticity fields are calculated with a least squares extrapolation. Unresolved velocity vectors are replaced with an 8-point weighted-average of the nearest neighbors. The vector field has been temporally smoothed with a 5-point running

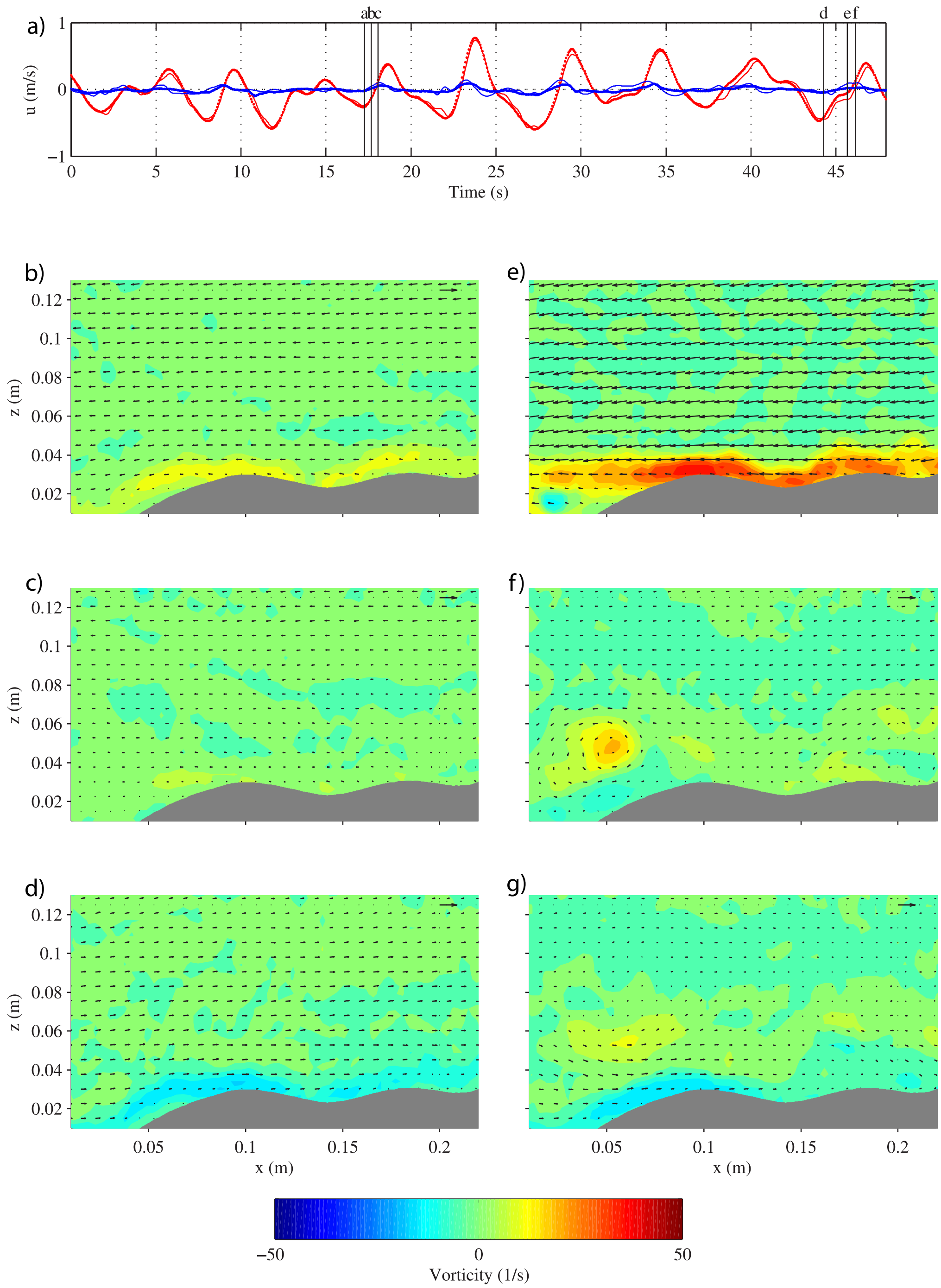

Figure 5. (a) A 48-s time series of horizontal (red) and vertical (blue) velocities as measured by the ADV (solid line) and PIV (dots) for the second realization. (b–g) Snapshots of the vorticity field (color scale), 3 Hz low-pass filtered velocity field (black vectors) at the six times indicated in the time series in Figure 5a. A 0.5 m/s scale vector is shown in the upper right corner. Onshore flow is directed to the right. Positive vorticity represents flows rotating in the counterclockwise direction.

average to reduce noise. An examination of the vorticity field for the offshore directed flow sequence in Figure 4 is shown in Figure 5. In the first sequence (Figures 5b–5d) regions of near-bed shear develop at peak offshore flow (Figure 5b) and at flow reversal (Figure 5d). However, no coherent structure forms away from the boundary. In the second sequence, during the peak of the offshore excursion, there exists a region of high near-bed counterclockwise-directed vorticity (Figure 5e). As the flow decelerates, the region of high vorticity is lifted into the water column (Figure 5f). Following ejection, the vortex is advected with the flow as it dissipates and loses its shape (Figure 5g).

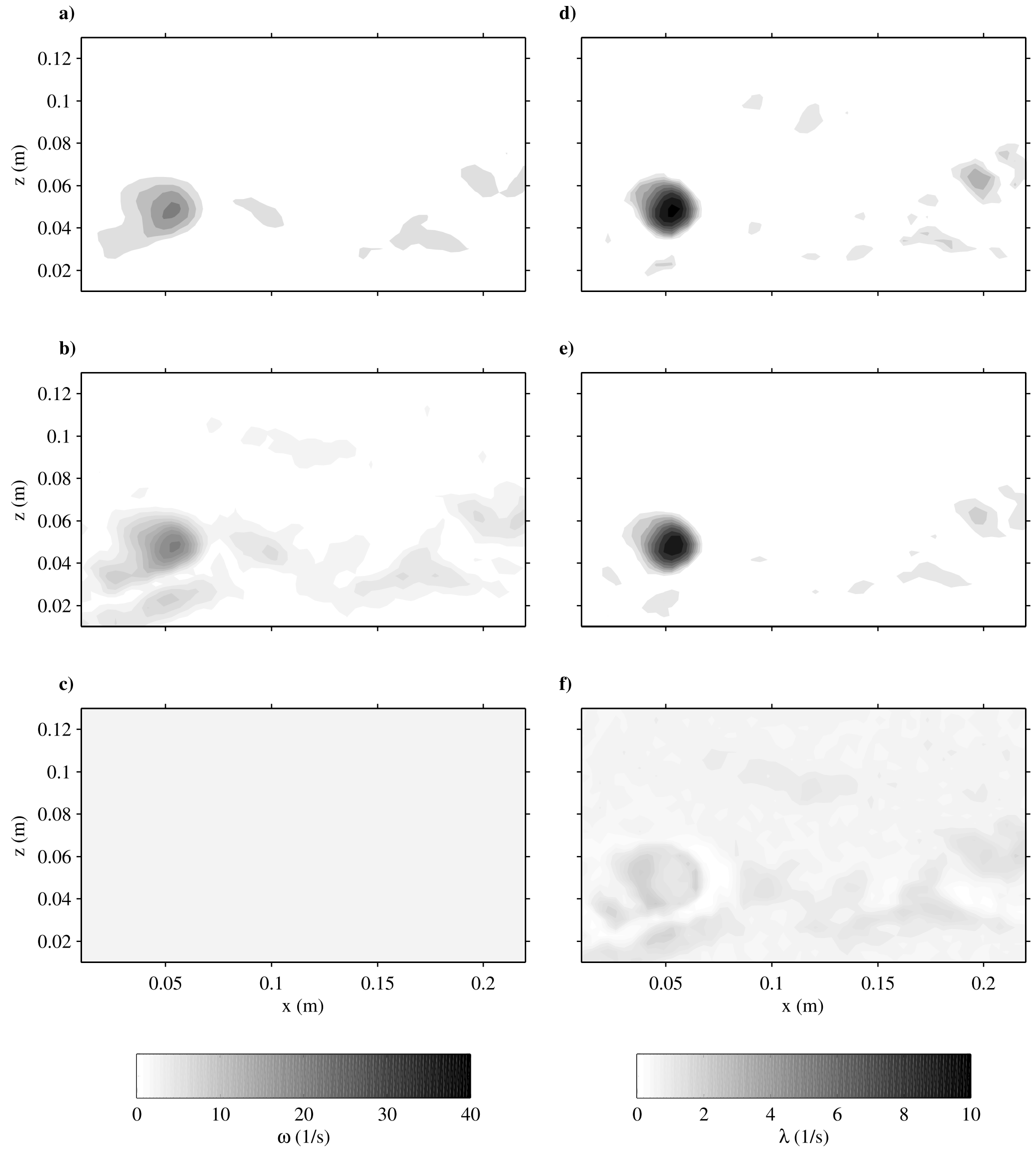

Figure 6. (a) The vorticity field and (d) swirling strength field of the image chosen for the Monte Carlo simulation. (b) The mean and (c) standard deviation of the vorticity calculated from perturbed velocity vectors. (e) The mean and (f) standard deviation of the swirling strength calculated from perturbed velocity vectors. The Monte Carlo simulation used to make the perturbations is described in the text. Onshore flow is directed to the right.

[12] In real fluids, the identification of such structures is complicated by diffusion and, in this case, boundary generated shear. Characterization is also complicated as random waves over movable rippled beds cannot easily be reduced to wave phase and an average ripple steepness (i.e., η_b/λ_b). Vorticity magnitude has been widely used to identify coherent vortical structures. However, this may not always be satisfactory since vorticity does not identify vortex cores in shear flow, especially if the background shear is comparable to the vorticity magnitude within the vortex [*Jeong and Hussain*, 1995]. Since a vortex core must exclude a wall, vorticity is not a suitable criterion for vortex identification in a boundary layer. In the following analysis, we characterize vortical structures with the swirling strength criterion defined by *Zhou et al.* [1999]. This criterion is based on the imaginary component of the eigenvalue, λ, of the velocity gradient tensor ($\mathbf{D}$), defined as

$$\mathbf{D} = \begin{bmatrix} \frac{\partial u}{\partial x} & \frac{\partial u}{\partial z} \\ \frac{\partial w}{\partial x} & \frac{\partial w}{\partial z} \end{bmatrix}. \tag{1}$$

In two dimensions, the characteristic equation is given by

$$\lambda^2 + P\lambda + Q = 0, \tag{2}$$

where the first invariant $P = -\mathrm{tr}(\mathbf{D})$ becomes

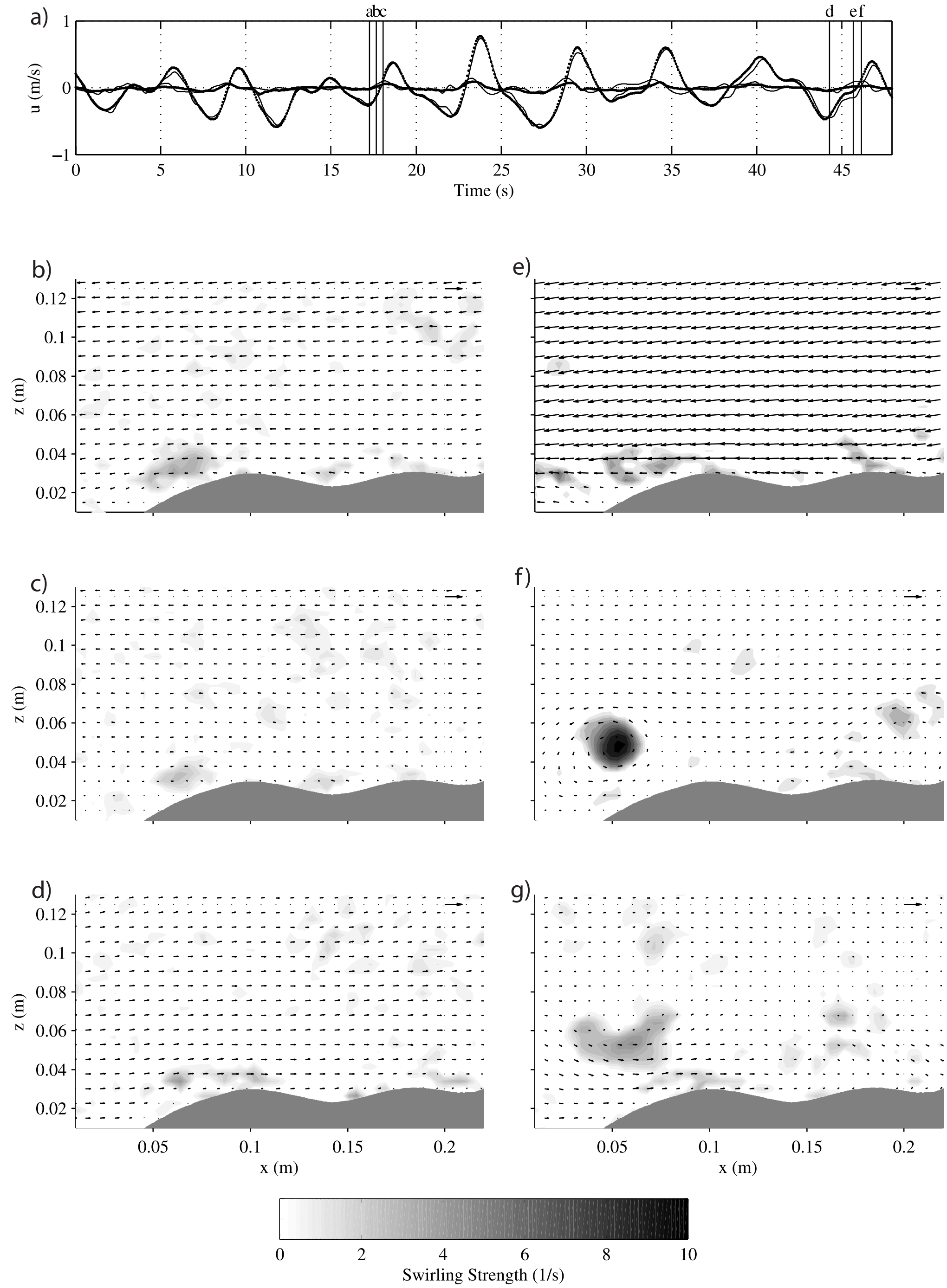

Figure 7. (a) A 48-s time series of horizontal and vertical velocities as measured by the ADV (solid line) and PIV (dots) for the second realization (see Figure 5 for colored direction differentiation). (b–g) Snapshots of the swirling strength field (black-and-white scale), 3 Hz low-pass filtered velocity field (black vectors) at the six times indicated in the time series in Figure 7a. A 0.5 m/s scale vector is shown in the upper right corner. Onshore flow is directed to the right.

$$P = -\left(\frac{\partial u}{\partial x} + \frac{\partial w}{\partial z}\right) \tag{3}$$

and the second invariant, $Q = \frac{1}{2}((P)^2 - tr((\mathbf{DD})^2))$. For incompressible flow, $P = 0$. Although generally small in this two-dimensional environment, P is retained to account for any mass entering and leaving the laser sheet in the alongshore plane. The swirling strength, $\lambda_{ci}(x, z, t)$, is defined as the complex component of the eigenvalue. Physically, as stated by *Chakraborty et al.* [2005], the swirling strength is a measure of the local twisting rate within a vortex. This method allows for easier spatial averaging in order to find the areas with the largest swirling

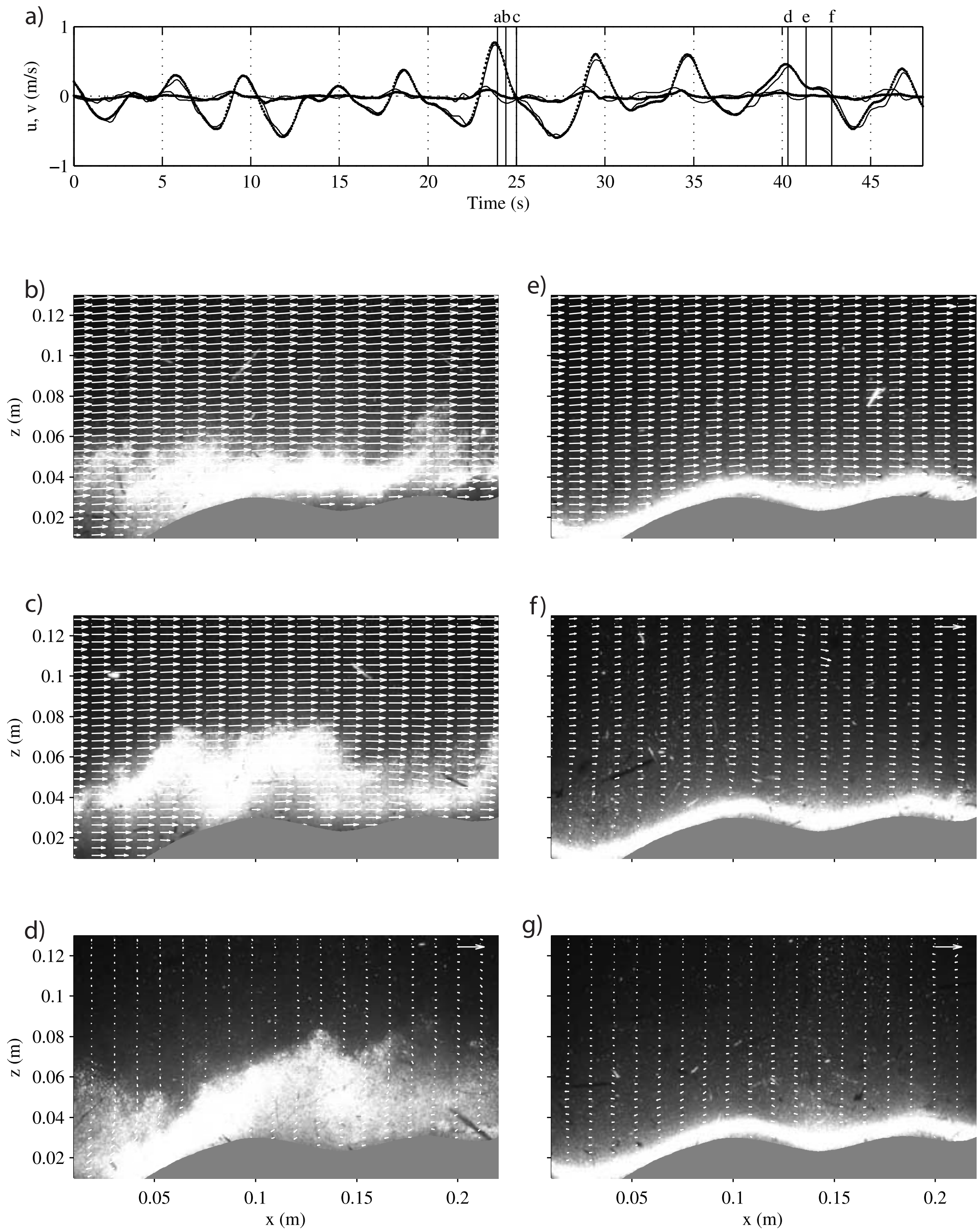

Figure 8. (a) A 48-s time series of horizontal and vertical velocities as measured by the ADV (solid line) and PIV (dots) for the second realization (see Figure 9 for colored direction differentiation). (b–g) Snapshots of the raw images and instantaneous velocity fields (white vectors) at the six times indicated in the time series Figure 8a. A 0.5 m/s scale vector is shown in the upper right of each image. Onshore flow is directed to the right.

strength without considering the near-bed shear. A Monte Carlo simulation of the vorticity and swirling strength parameters for the coherent structures present in Figures 4f and 5f was performed to examine how the propagation of errors in the velocity field will affect these quantities. The velocity field was perturbed with normally distributed random variables scaled with a defined amplitude. This amplitude was defined as ± the standard deviation of the uppermost row of calculated velocity vectors. For the velocities shown in Figure 4f the amplitude was 0.017 m. Figure 6 shows the mean values of the vorticity and λ_{ci} (Figures 6b and 6e). These reveal similar values to that of the instantaneous vorticity field shown in Figure 5f, reproduced in Figure 6a and that of the instantaneous λ_{ci} field of the same point in time shown in Figure 6d. Also, the standard deviation values of the vorticity and λ_{ci} (Figure 6c and 6f) are low showing little error propagation.

[13] An examination of the swirling strength field for the offshore directed flow sequence in Figure 4 is shown in Figure 7. In the first sequence (Figure 7b–7d) no noticeable regions of high swirling strength are evident, including near the bed where there were areas of high vorticity. In the

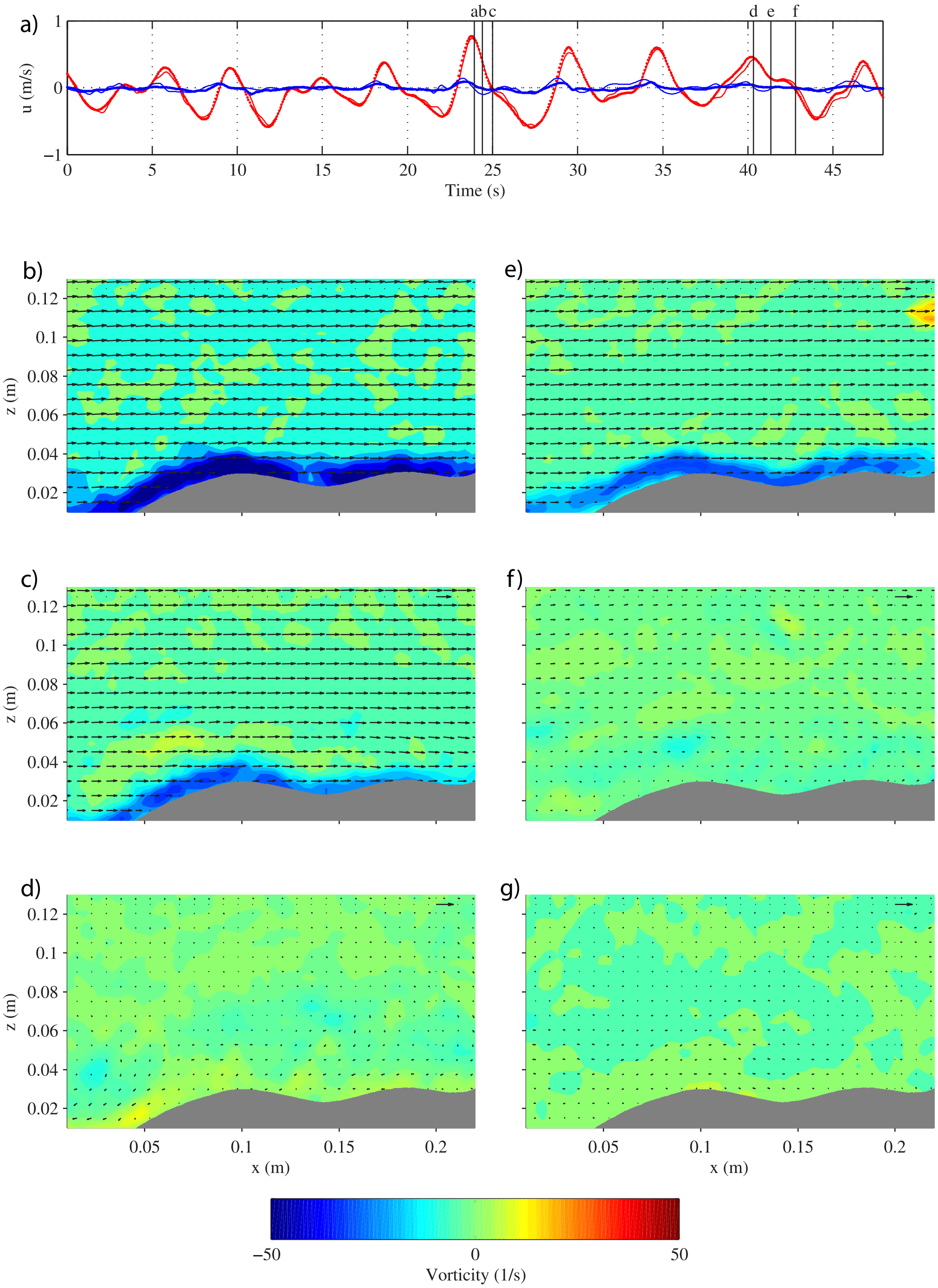

Figure 9. (a) A 48-s time series of horizontal (red) and vertical (blue) velocities as measured by the ADV (solid line) and PIV (dots) for the second realization. (b–g) Snapshots of the vorticity field (color scale), 3 Hz low-pass filtered velocity field (black vectors) and at the 6 times indicated in the time series in Figure 9a. A 0.5 m/s scale vector is shown in the upper right corner. Onshore flow is directed to the right. Positive vorticity represents flows rotating in the counterclockwise direction.

second sequence, as the flow decelerates (Figure 7f), a region of high swirling strength is evident over the most-offshore ripple at the steep slope (x = 0.05 m). As the flow reverses (Figure 7g), the high swirling strength region is advected and dissipates.

[14] Figures 8, 9, and 10 show the flow field and image, vorticity field, and swirling strength field evolution through two separate onshore directed flow excursions. As before, each sequence consists of the peak onshore flow (Figures 8b and 8e, 9b and 9e, and 10b and 10e) followed by flow deceleration (Figures 8c and 8f, 8c and 9f, and 10c and 10f), and flow reversal (Figures 8d and 8g, 9d and 9g, and 10d and 10g). In the first sequence, the peak onshore velocity reaches 0.71 m/s over a 1/2 wave excursion of 2 s

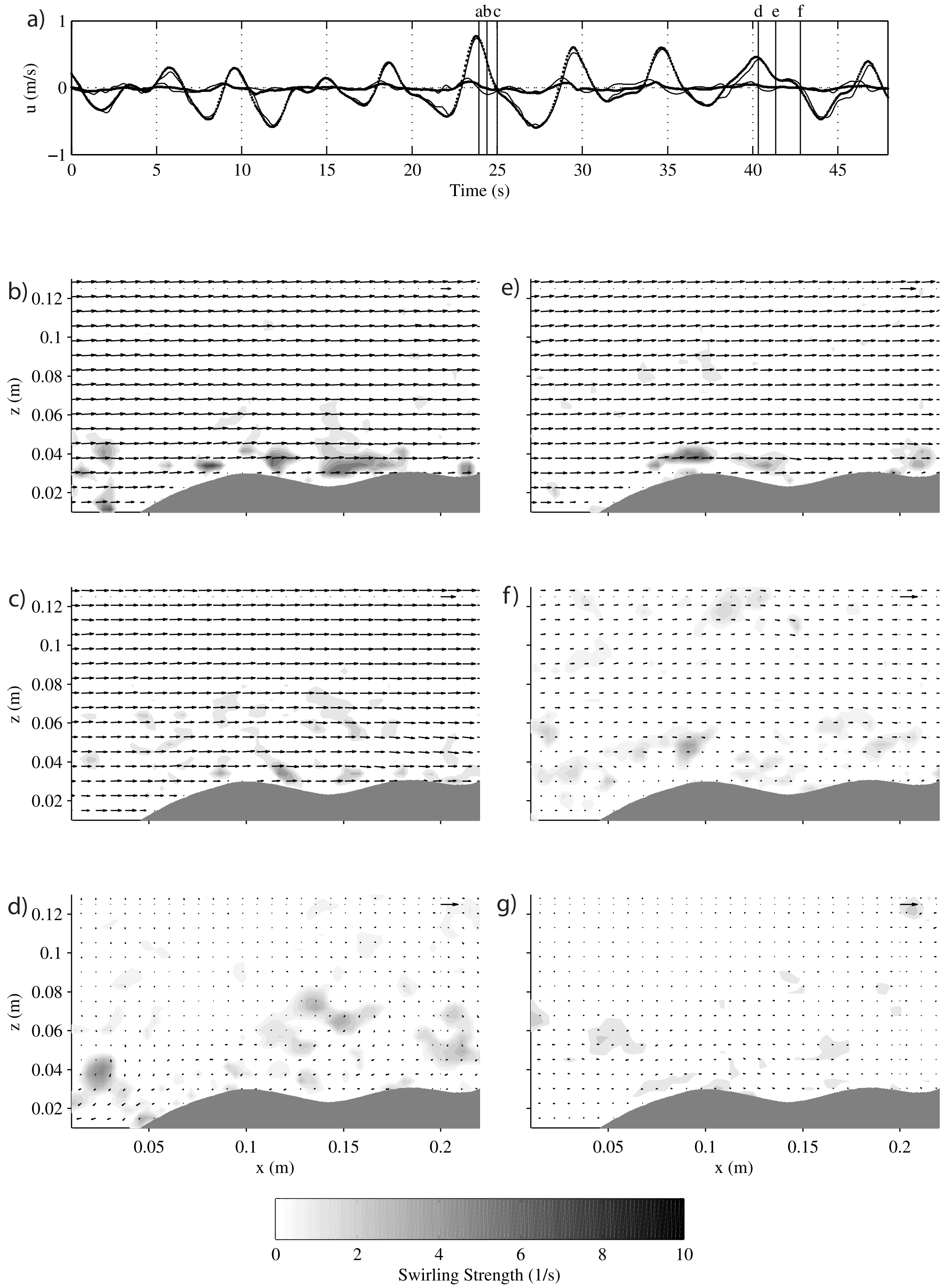

Figure 10. (a) A 48-s time series of horizontal and vertical velocities as measured by the ADV (solid line) and PIV (dots) for the second realization (see Figure 9 for colored direction differentiation). (b–g) Snapshots of the swirling strength field (black-and-white scale), 3 Hz low-pass filtered velocity field (black vectors) at the 6 times indicated in the time series in Figure 10a. A 0.5 m/s scale vector is shown in the upper right corner. Onshore flow is directed to the right.

(Figures 8b–8d, 9b–9d, and 10b–10d). The images show a significant entrainment of sediment that is present throughout the entire quarter wave period over the entire bed form (Figures 8b–8f). The shields parameter during peak flow reaches 0.8 and is within the sheet flow regime [*Foster et al.*, 2006]. The vorticity is high during peak flow and in the initial phase of deceleration yet no significant vortex is identified in the swirling strength, once again consistent with a sheet flow phenomenon. In the second sequence, the peak onshore velocity only reaches 0.37 m/s over a 1/2 wave excursion of 4.3 s (panels (e)–(g)). The magnitude of forcing is consistent with the offshore sequence in Figures 4e–4g. In this sequence, there is only a small amount of sediment entrained in the trough present at x = 0.14 m (Figures 8f

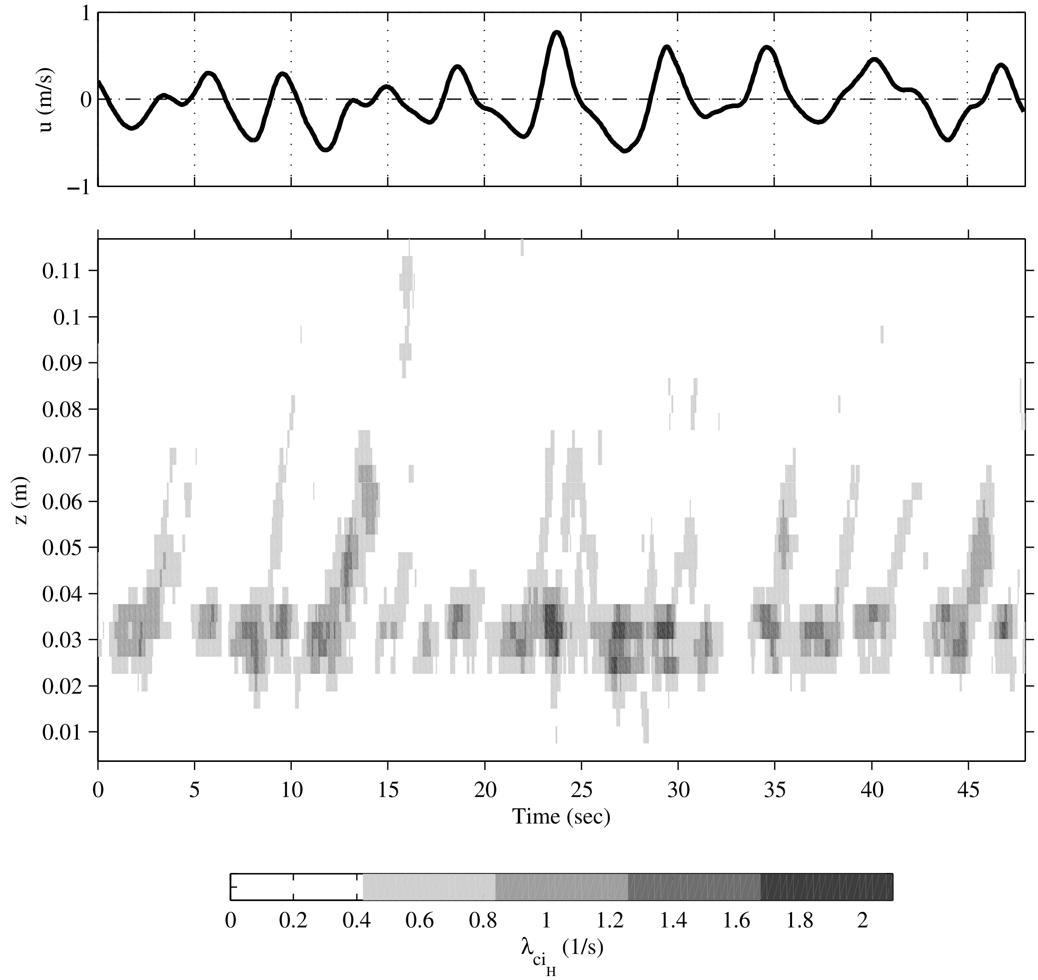

Figure 11. A time series of (top) the ADV horizontal free stream velocity and (bottom) the horizontally averaged swirling strength, λ_{ci_H} for the second realization.

and 8g). This would suggest that the nonsymmetrical ripple acts as a forward facing step during onshore directed flow and a backward facing step with a large trough vortex during offshore directed flow.

[15] An advantage of the swirling strength characterization is that it allows for spatial averaging without the need to artificially eliminate the boundary shear. The temporal evolution of the swirling strength is examined as a function of elevation by defining the horizontally averaged swirling strength, λ_{ci_H}, with

$$\lambda_{ci_H}(z,t) = \frac{1}{x_2 - x_1}\int_{x_1}^{x_2} \lambda_{ci}(x,z,t)dx, \quad (4)$$

where x_1 = 0 m and x_2 = 0.23 m. As this is a spatially averaged quantity, the magnitude will be lower than the local peaks in the swirling strength. The horizontally averaged swirling strength for the second realization is shown in Figure 11. The large-magnitude signals present in the near-bed region ($0.025 < z < 0.04$ m) are indicative of forming vortical structures. During the longer-duration excursions, λ_{ci_H} often increases in magnitude as the structure builds strength until the flow reverses (i.e., $12.5 < t < 14$ s). In this realization, several near-bed vortex generations are followed by vertically sloping swirling strength at $z \geq 0.04$ m and is evidence of vortex ejection. This characterization suggests a vortex ejection from $43 < t < 45$ s and is consistent with Figure 4.

[16] An estimate of the temporal duration of vortex generation was manually identified by high swirling in the near-bed region (see horizontal lines in Figure 12). This approximation allows for the examination of the hydrodynamic-forcing conditions present during generation. The hydrodynamic forcing involved in the generation of the vortical structures is examined with an estimate of the Reynolds number, *Re*, and Keulegan-Carpenter number, *KC*. Following *Hara and Mei* [1990] and *Ourmieres and Chaplin* [2004], *Re* is characterized with

$$Re = \frac{|u_o|u_o T_{1/2}}{2\pi\nu}, \quad (5)$$

where u_o is the peak velocity within a single one-half wave and $T_{1/2}$ is twice the duration between each zero-crossing. *KC* is characterized with

$$KC = \frac{u_o T_{1/2}}{\eta}, \quad (6)$$

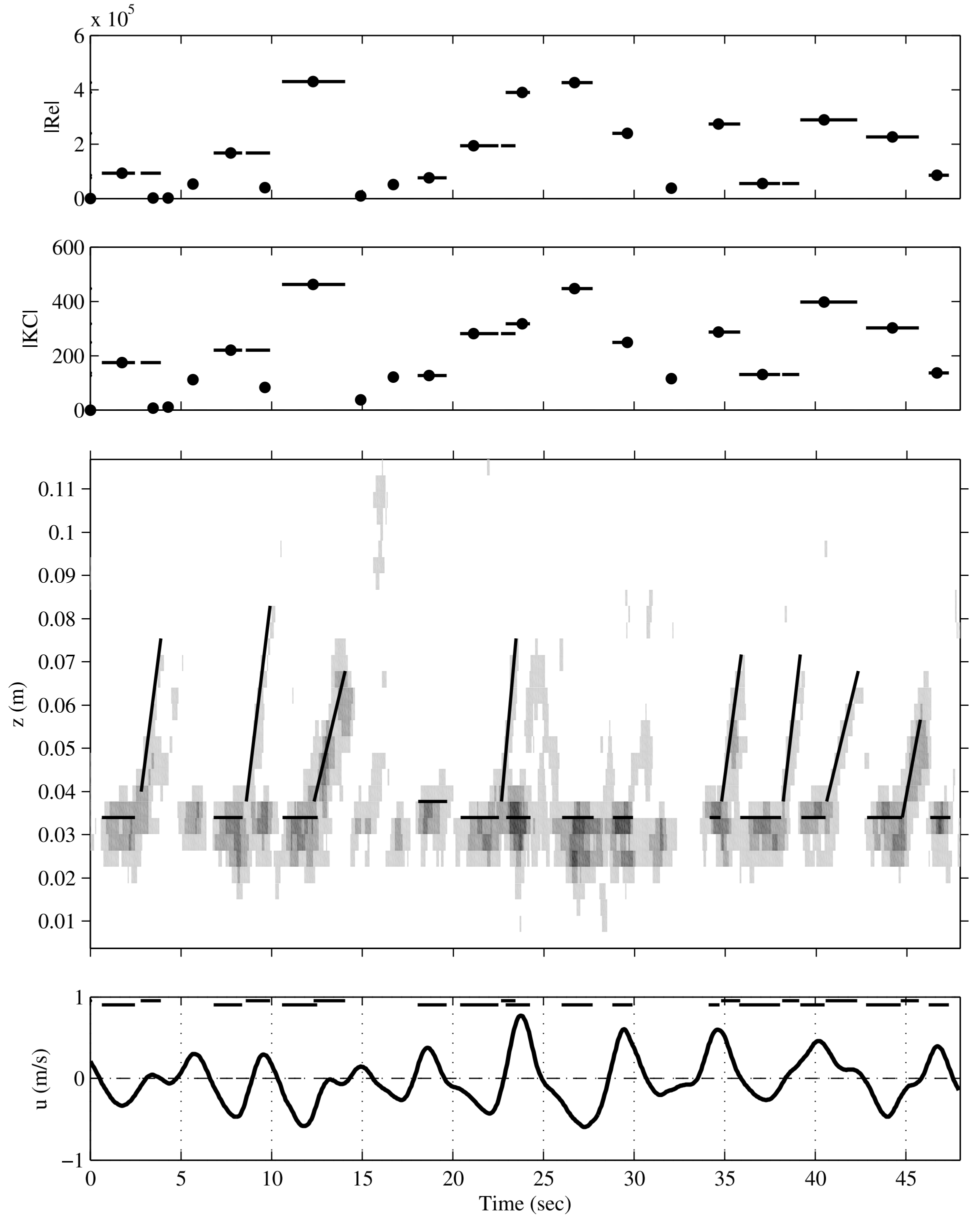

Figure 12. A time series of (fourth plot) the ADV horizontal free stream velocity, (third plot) the horizontally averaged swirling strength, and (first and second plots) the absolute value of the Reynolds number and Keulegan-Carpenter number for each $T_{1/2}$ for the second realization. The black lines superimposed on the swirling strength show occurrences of vortex generation and ejection, respectively. The black lines superimposed on the velocity time series at 0.9 and 0.95 m/s and on the Reynolds numbers and Keulegan-Carpenter number show the temporal excursion for each of the vortex generation and ejection events. The colorbar is consistent with Figure 11.

where η is the ripple height. In these formulations, Re and KC are signed quantities allowing for the examination of vortex generation as a function of flow direction. Figure 12 shows the variability of $|Re|$ and $|KC|$ for the second realization. In general, vortex generation is present for the larger $|Re|$ and $|KC|$. Not surprisingly, the duration of vortex generation (i.e., high swirling from $0.02 < z < 0.07$ m) is longer for the longer durations of offshore-directed flow than for the shorter duration of onshore-directed flow.

[17] As discussed above, λ_{ci} also shows evidence of vortex ejection. The ejecting structures show an upward slope of nonnegligible swirling that follows high swirling in the near-bed region ($0.03 < z < 0.04$ m) (see the vertically sloped lines on Figure 12). Interestingly, the two events with the strongest ejection signal (t = 12.5 and 43 s) occur when the onshore velocity, following the half-wave period of vortex generation, is relatively small. The vertical velocity of the ejected structure is calculated as the slope of each vertical line. The ejection velocities vary from 0.02 to 0.05 m/s in the upward direction.

[18] The horizontal position of vortex generation is examined with the temporal evolution of the near-bed swirling

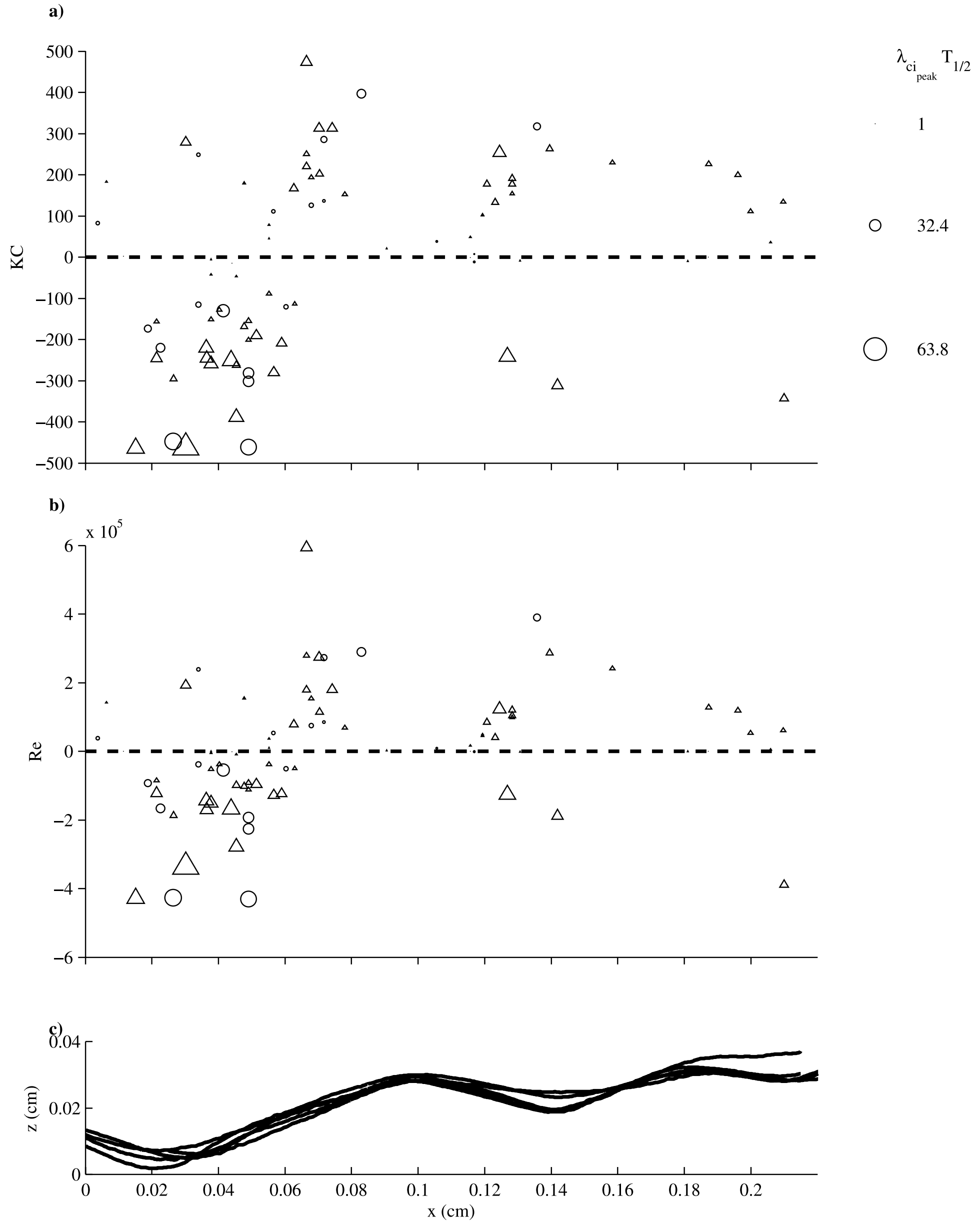

Figure 13. (a) Keulegan-Carpenter number and (b) the Reynolds number during the maximum swirling event normalized by twice the duration between each zero crossing, $T_{1/2}$, at the horizontal location of the event (circle, realization 2; triangle, realizations 1, 3, 4, 5). The size of the symbol corresponds to the swirling strength of the event multiplied by $T_{1/2}$, as shown in the legend in the upper right corner. (c) The centroid bed form profiles for each realization shifted to match the ripple peak at x = 0.09 m of the second realization.

strength by defining the vertically averaged swirling strength, λ_{ci_V}, with

$$\lambda_{ci_V}(x,t) = \frac{1}{(z_b + 0.02m) - z_b} \int_{z_b}^{z_b+0.02m} \lambda_{ci}(x,z,t)dz, \quad (7)$$

where z_b is the elevation of the centroid of the light reflected from the bed. For each one-half wave period, a maximum value, $\lambda_{ci_{peak}}$, time period, $T_{1/2}$ and horizontal position where $\lambda_{ci_V} = \lambda_{ci_{peak}}$ is determined. The horizontal position of vortex generation for the five realizations and the range of *KC* and *Re* are shown in Figures 13a and 13b. For comparison purposes, each of the realizations has been horizontally offset to be aligned with the first realization. Please note the size of individual symbols scales with the peak swirling strength, $\lambda_{ci_{peak}}$, nondimensionalized by $T_{1/2}$, and is shown in the upper right corner. The largest events (i.e., highest $\lambda_{ci_{peak}} T_{1/2}$) occur during the offshore excursions. During offshore-directed flows (negative values of *KC* and *Re*), the largest vortical structures occur on the downslope side of the ripple, offshore of the ripple crest, roughly between $0.01 < x < 0.06$ m. During onshore-directed flows, $\lambda_{ci_{peak}} T_{1/2}$ is lower and the vortical structures occur onshore of the ripple crest between $0.09 < x < 0.14$ m, but also more

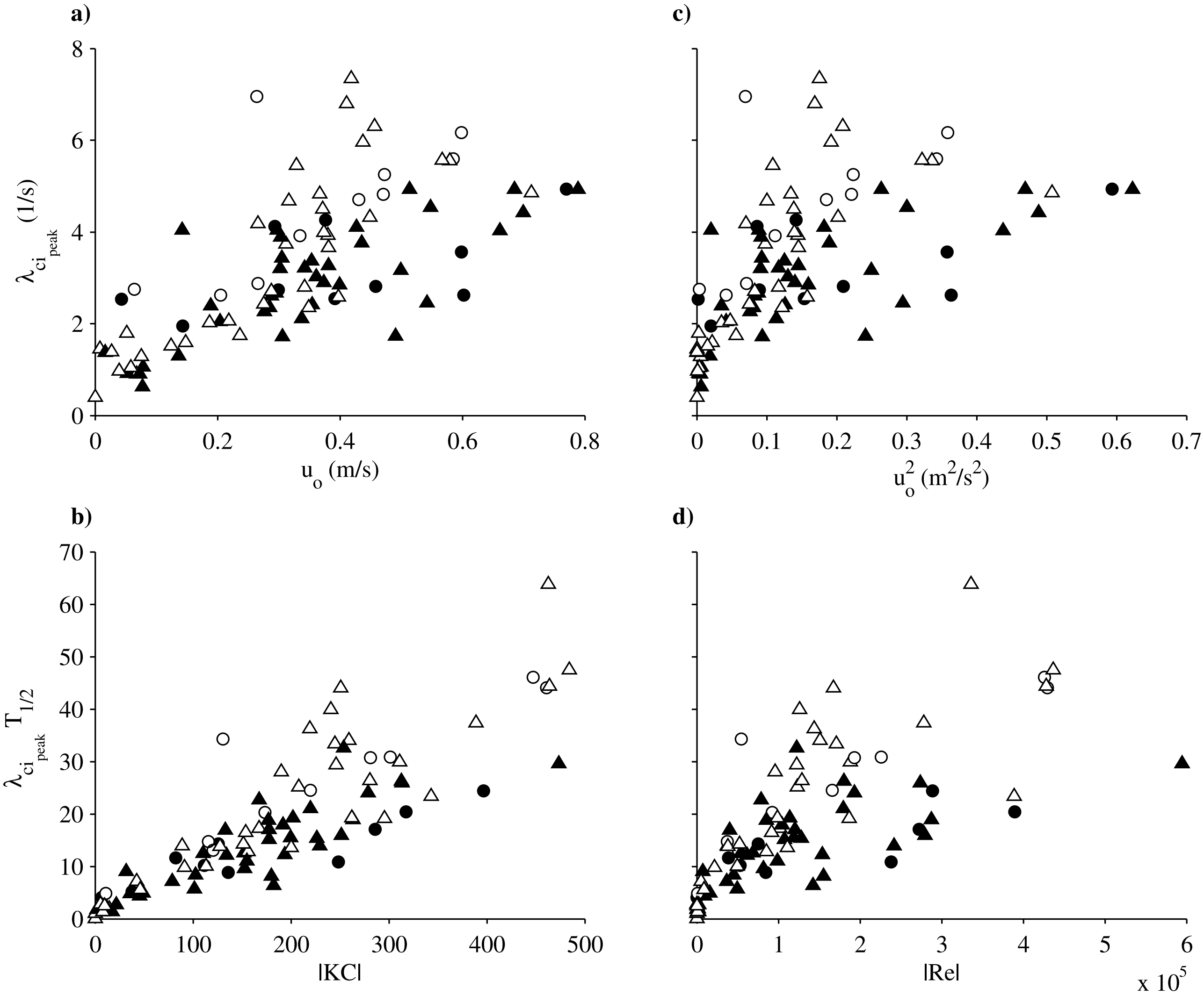

Figure 14. (top) Peak swirling strength and corresponding (a) horizontal velocity or (b) horizontal velocity squared for each half wave period. (bottom) Peak swirling strength nondimensionalized by $T_{1/2}$ and corresponding (c) $|KC|$ or (d) $|Re|$ for each half wave period (circle, realization 2; triangle, realizations 1, 3, 4, 5). The open and solid symbols represent vortex generation events during offshore and onshore flow, respectively.

frequently just offshore of the ripple crest. A closer examination of the structure formed on the offshore slope during onshore flow suggests that these events are small near-bed structure that occur during peak flow (see Figures 10b and 10e). These observations provide further evidence that the deep trough and ripple crest are acting as a backward facing step during offshore excursions and a forward facing step during onshore excursions.

[19] Figure 14 illustrates the strong dependence of vortex generation (defined dimensionally with $\lambda_{ci_{peak}}$ or nondimensionally with $\lambda_{ci_{peak}} T_{1/2}$) on the hydrodynamic forcing (defined dimensionally with u_o or u_o^2 or nondimensionally with $|KC|$ or $|Re|$). Figure 14b shows the strongest trend of $\lambda_{ci_{peak}} T_{1/2}$ with $|KC|$. Despite the nonsymmetric bed form, both onshore and offshore directed flows show a trend with $|KC|$ (although the offshore directed events are larger). This trend is less obvious for $|Re|$ and would suggest a lower dependence on the wave velocity. According to *Zhou et al.* [1999], the time for a structure to complete a single revolution is $\frac{2\pi}{\lambda_{ci}}$. Vortices that complete a revolution in less than a half-wave duration would then require that $\lambda_{ci} T_{1/2} > 4\pi$. In Figure 14 $\lambda_{ci_{peak}}$ has been filtered through vertical averaging, therefore this critical limit should be lower.

4. Discussion

[20] The relationship shown in Figure 14 is significant for several reasons. First, it suggests the presence or absence of vortex structures for a given bed form shape may be purely characterized with the free stream horizontal velocity realization. Intuition would suggest that an upper limit of *KC* and *Re* would exist. If these nondimensional numbers are increased beyond that upper limit, then, at some point, the bed would flatten. Second, if sediment is entrained in the structures, as these observations suggest, then it may be possible to examine *Re* or *KC* dependence with the large

range of suspended sediment vertical profile observations that currently exist.

[21] Finally, it provides questions pertaining to how smaller laboratory experiments may or may not be translated to field-scale environments. These studies often incorporate sinusoidal waves and symmetrical fixed ripples [*Sand Jespersen et al.*, 2004; *Earnshaw and Greated*, 1998]. In the work by *Sand Jespersen et al.* [2004], a single symmetric ripple oscillated in otherwise still fluid showed vortex evolution over single wave periods. They showed peak circulation which occurs just prior to flow reversal (170°) and is generally consistent with vortex ejection during offshore flow shown in Figures 7e–7g. However, the two structures differ in that our observations show no evidence of the vortex bending over the ripple crest following flow reversal. *Earnshaw and Greated* [1998] also do not show evidence of the ejected vortex being advected down into the next trough. Our observations are consistent with the ejection mechanism identified by *Earnshaw and Greated* [1998]. However, the velocities in our study are significantly larger and more quickly dissipate the vortices.

5. Conclusions

[22] Observations of the two-dimensional flow field over a natural sand bed have been obtained in a full-scale random wave environment. The observations are obtained with a submersible PIV system. Two-dimensional velocity fields are estimated over a 0.23×0.23 m^2 area. Five 48-s realizations are used to examine vortex generation and ejection over a rippled bed. Over the course of the sampling period the bed form migrated between 0.0001 to 0.0005 m/s in the onshore direction. The observed boundary layer thickness over this mobile bed of roughly 0.025 m is consistent with the boundary layer thickness predicted by the semiempirical model of *Madsen* [1994], if the roughness is parameterized with the grain roughness. However, if the roughness is parameterized with the rippled bed geometry, the model thickness prediction is considerably greater than the observed thickness.

[23] The dynamics of vortex generations are characterized with the swirling strength model of *Zhou et al.* [1999]. Contours of swirling strength are consistent with estimates of vorticity and allow for an identification of the generation and ejection of individual events. An examination of the swirling strength over consecutive one-half wave segments shows that higher swirling strength events occur with increasing *KC*.

[24] Once a vortex has formed, the ejection of the vortex is a function of the fluid characteristics following generation. A mild deceleration allows a vortex to lift into the water column and be advected. However, a steep deceleration restricts the vertical advancement of a vortex causing it to dissipate and not be advected. These results also suggest that the vortex ejection may be dependent on the local bed form slope. In these observations, most of the vortex ejections occur as the flow reverses direction to onshore-directed flow. This would suggest that sediment is lifted over the bed form crest and is consistent with onshore migration of the ripples. These observations suggest that the generation and ejection of vortex structures may be predictable functions of the free-stream hydrodynamics and ripple geometry.

[25] **Acknowledgments.** This work was supported by the National Science Foundation (OCE-0351903, CTS-0348203). C. Nichols and D. Foster gratefully acknowledge the O. H. Hinsdale Research Laboratory staff and students. Also, this work would not have been possible without assistance from Ohio State University Coastal Transport Lab (G. Smith, K. Halton, and H. Smith). A special thank you goes to Lili Yu for her statistical consulting. We also acknowledge the insight provided by B. M. Sumer and the anonymous reviewers.

References

Adrian, R. J. (1991), Particle-imaging techniques for experimental fluid mechanics, *Annu. Rev. Fluid Mech.*, *23*, 261–304.
Adrian, R. J. (2005), Twenty years of particle image velocimetry, *Exp. Fluids*, *39*, 159–169.
Ahmed, A. S. M., and S. Sato (2001), Investigation of bottom boundary layer dynamics of movable bed by using enhanced piv technique, *Coastal Eng. J.*, *43*(4), 239–258.
Bagnold, R. A. (1946), Motion of waves in shallow water, interaction between waves and sand bottoms, *Proc. R. Soc., Ser. A*, *187*, 1–18.
Chakraborty, P., S. Balachandar, and R. J. Adrian (2005), On the ralationships between local vortex identification schemes, *J. Fluid Mech.*, *535*, 189–214.
Chang, Y. S., and D. M. Hanes (2004), Suspended sediment and hydrodynamics above mildly sloped long wave ripples, *J. Geophys. Res.*, *109*, C07022, doi:10.1029/2003JC001900.
Cowen, E. A., I. M. Sou, P. L. Liu, and B. Raubenheimer (2003), Particle image velocimetry measurements within a laboratory-generated swash zone, *J. Eng. Mech.*, *129*(10), 1119–1129.
Darwin, G. H. (1883), On the formation of ripple-mark in sand, *Proc. R. Soc.*, *36*, 18–43.
Earnshaw, H. C., and C. A. Greated (1998), Dynamics of ripple bed vortices, *Exp. Fluids*, *25*, 265–275.
Efron, B., and R. J. Tibshirani (1993), *An Introduction to the Bootstrap*, CRC Press, Boca Raton, Fla.
Foster, D. L., R. A. Beach, and R. A. Holman (2000), Field observations of the wave bottom boundary layer, *J. Geophys. Res.*, *105*(C8), 19,631–19,648.
Foster, D. L., A. J. Bowen, R. A. Holman, and P. Natoo (2006), Field evidence of pressure gradient induced incipient motion, *J. Geophys. Res.*, *111*, C05004, doi:10.1029/2004JC002863.
Foster, D. L., P. Natoo, T. P. Stanton, and J. Fredsøe (2007), The suspension of sediment from flat and megarippled beds: A pairing of models and observation, *Cont. Shelf Res.*, in press.
Grant, W. D., and O. Madsen (1979), Combined wave and current interaction with a rough bottom, *J. Geophys. Res.*, *84*(C4), 1797–1808.
Grant, W. D., and O. Madsen (1982), Movable bed roughness in unsteady oscillatory flow, *J. Geophys. Res.*, *87*(C1), 469–481.
Hara, T., and C. C. Mei (1990), Centrifugal instability of an oscillatory flow over periodic ripples, *J. Fluid Mech.*, *217*, 1–32.
Honji, H., A. Kaneko, and N. Matsunaga (1980), Flows above oscillatory ripples, *Sedimentology*, *27*, 225–229.
Jeong, J., and F. Hussain (1995), On the identification of a vortex, *J. Fluid Mech.*, *285*, 69–94.
Madsen, O. (1994), Spectral wave-current bottom boundary layer flows, paper presented at 24th International Conference on Coastal Engineering, Am. Soc. of Civ. Eng., Reston, Va.
Nakato, T., F. A. Locher, J. R. Glover, and J. F. Kennedy (1977), Wave entrainment of sediment from rippled beds, *J. Waterw. Port Coastal Ocean Eng.*, *103*(WW1), 83–99.
Nimmo Smith, W. A. M., P. Atsavapranee, J. Katz, and T. R. Osborn (2002), PIV measurements in the bottom boundary layer of the coastal ocean, *Exp. Fluids*, *33*, 962–971.
Nimmo Smith, W. A. M., J. Katz, and T. R. Osborn (2004), On the structure of turbulence in the bottom boundary layer of the coastal ocean, *J. Phys. Oceanogr.*, *35*, 72–92.
Osborne, P. D., and C. E. Vincent (1996), Vertical and horizontal structure in suspended sand concentrations and wave-induced fluxes over bedforms, *Mar. Geol.*, *131*, 195–208.
Ourmieres, Y., and J. R. Chaplin (2004), Visualizations of the disturbed-laminar wave-induced flow above a rippled bed, *Exp. Fluids*, *36*, 908–918.
Rockwell, D., C. Magness, and J. Towfighi (1993), High image-density particle image velocimetry using laser scanning techniques, *Exp. Fluids*, *14*, 181–192.

Sand Jespersen, T., J. Q. Thomassen, A. Andersen, and T. Bohr (2004), Vortex dynamics around a solid ripple in an oscillatory flow, *Eur. Phys. J.*, *38*, 127–138.
Smyth, C., A. E. Hay, and L. Zedel (2002), Coherent Doppler Profiler measurements of near-bed suspended sediment fluxes and the influence of bed forms, *J. Geophys. Res.*, *107*(C8), 3105, doi:10.1029/2000JC000760.
Sveen, J. K. (2004), An introduction to MatPIV 1.6.1, 2nd ed., report, pp. 1–27, Department of Mathematics, Univ. of Oslo, Oslo.
Thorne, P. D., and D. M. Hanes (2002), A review of acoustic measurement of small-scale sediment processes, *Cont. Shelf Res.*, *22*, 603–632.
Willert, C. E., and M. Gharib (1991), Digital particle image velocimetry, *Exp. Fluids*, *10*, 181–193.
Zhou, J., R. J. Adrian, S. Balachandar, and T. M. Kendall (1999), Mechanisms for generating coherent packets of hairpin vortices in channel flow, *J. Fluid Mech.*, *387*, 353–396.

D. L. Foster and C. S. Nichols, Department of Civil and Environmental Engineering and Geodetic Science, Ohio State University, Columbus, OH, 43210-1275, USA. (foster.316@osu.edu; nichols.236@osu.edu)